Supporting Information

Using -NH and -OH Rich Organic Cathode to Explore Proton Transport in Aqueous Zinc-Ion Batteries

Wenlong Zhang,[a] Suyan Niu,[a] Yao Wang,[a] Zhenyu Wang,[a] Yiming Wang,[a] Na Ju,[a] Xinyu Liu, Yinggang Jia *[a] and Hongbin Sun *[a]

Department of Chemistry, Northeastern University, Shenyang 110819, People's Republic of China.

E-mail: sunhb@mail.neu.edu.cn; jiayinggang@mail.neu.edu.cn

Contents

1.Experimental Section

1.1 Chemicals and Materials

Iron chloride hexahydrate ($FeCl_3 \cdot 6H_2O$, AR, 99%), Protocatechualdehyde ($C_7H_6O_3$, AR, 99%), and o-phenylenediamine (oPD, AR, 99.5%) were purchased from Shanghai Aladdin Biochemical Technology Co., Ltd. Ti mesh, Ketjin black (ECP-600JD) and zinc foil (0.2 mm, 99.99%) were obtained from Canrd Technology Co. Ltd, polytetrafluoroethylene (PTFE, 60 wt%) and phosphomolybdic acid (AR) were provided by Shanghai Macklin Biochemical Technology Co., Ltd; $ZnSO_4 \cdot 7H_2O$ (99%) was purchased from Sinopharm Chemical Reagent Co. ,Ltd. All the chemicals were used as received without any further purification.

1.2 Synthesis of 2,3-Diaminophenazine (DAP)

The synthesis method of DAP, based on the literature, [1] 50 mL $FeCl_3$ solution is rapidly added into 250 mL of 0.02 M oPD solution and stirred for 10 minutes. The color changes from black to bright red during the reaction, and ultimately, a substantial amount of reddish-brown precipitate forms. This precipitate is left undisturbed for 5 hours. Subsequently, the solid is separated by filtration, washed three times with water and ethanol respectively, and dried to obtain the product named DAP.

1.3 Synthesis of 4-(1H-imidazo[4,5-b] phenazine-2yl) benzene-1,2diol (PD)

The synthesis of PD involves a cyclization reaction between the ortho-amino group and aldehyde group, as depicted in the S1. Initially, 0.42 g (2 mmol) of DAP and 0.35 g (2.5 mmol) of protocatechualdehyde were reacted in DMF at 120 ℃ for 48 hours. Subsequently, the reaction mixture was diluted with a substantial amount of cool deionized water, followed by centrifugation to obtain the solid product which was further washed three times with water and ethanol through centrifugation.[2]

1.4 Synthesis of 2-((3-aminophenazin-2-yl) amino)-5-(1H-imidazo[4,5-b] phenazine-2-yl) phenol (APIPP)

The APIPP compound was synthesized by subjecting 0.328 g (1 mmol) of PD and 0.252 mg (1.2 mmol) of DAP for further dehydration and condensation in DMF and at120 ℃, with the addition of 60 mg phosphomolybdic acid for a duration of 48 hours. Subsequently, the reaction mixture was filtered while still hot, followed by three consecutive washes with acetone and ethanol to obtain the solid product APIPP, which was subsequently dried.

2． Electrode preparation and measurements

The preparation of APIPP-based electrodes for general testing involves several steps. Firstly, the active material APIPP, conductive agent Ketjen Black, and binder PTFE (10% aqueous solution) are mixed in a ratio of 6:3:1 by weight in isopropanol as the dispersant. The mixture is then ground into a paste and combined with a current collector titanium mesh using roll-to-roll method. Subsequently, the assembly is dried in a vacuum oven for 6 hours before being cut into electrode pieces using a cutting

machine. To ensure strong adhesion between materials and smooth surface finish without any protrusions piercing through the separator causing short circuits, the cut electrode pieces are further pressed. The resulting electrodes have an approximate loading capacity of 1-2 $mg \cdot cm^{-2}$. These prepared electrodes serve as positive electrodes, double-layer qualitative filter paper acts as separators, and zinc foil serves as negative electrodes to assemble coin cells. An aqueous solution of 70 μL 2 M $ZnSO_4$ was used as electrolyte, and the tests of electrochemical performance were conducted on Land system within voltage limits of 0.01-1.8 V during room temperature. Furthermore, Cyclic Voltammetry (CV) and Electrochemical Impedance Spectroscopy (EIS) tests were conducted on CHI660E electrochemical workstation to analyze their performance characteristics.

3. Material characterization

3.1Testing equipment and techniques

^1H NMR at 600 MHz (Bruker 600MHz) elucidates the structure of synthesized samples. Powder XRD, employing Cu Kα radiation, is executed on a Panalytical Empyrean diffractometer. Scanning Electron Microscopy (SEM) and Energy-Dispersive X-ray Spectroscopy (EDS) mapping were conducted for elemental analysis at 5 kV and 15 kV using the Tescan MAIA3 XMH instrument. TEM and EDS, at 200 kV, offer detailed insights (JEM2100PLUS, Japanese Electronics Corporation). FT-IR spectra of samples and electrodes in various states are obtained using a Bruker Vertex spectrometer with a KBr pellet. XPS spectra, collected with a Thermo Scientific K-Alpha, undergo elemental binding energy analysis, confirming C1s at 284.8 eV. Data processing utilizes the XPSPEAK software for comprehensive analysis.

3.2 Redox kinetics measurements

The relative contributions of surface capacitance control and diffusion control processes at different scanning rates can be quantified using the following equation:

$$i(v) = k_1 v + k_2 v^{\frac{1}{2}} \quad (1)$$

where $k_1 v$ represents the influence of surface capacitance control and $k_2 v^{1/2}$ represents the contribution from ion diffusion control.

$$i = a\, v^{\,b} \quad (2)$$

$$lg\, i = b\, lg\, v + lg\, a \quad (3)$$

In order to further ascertain the chemical kinetics behavior of the battery, we calculated the b value using the above equation. Among them, i represents the current (mA) at a specific potential, v denotes the scan rate ($mV \cdot s^{-1}$), and a is a constant. The obtained b value can be used to classify electrochemical reactions based on surface capacitance and diffusion control processes. When the b value is 0.5, electrode materials exhibit battery characteristics; when it ranges from 0.5 to 1, electrode materials display both battery and pseudocapacitive characteristics; when the b value equals 1, electrode materials demonstrate pseudocapacitive characteristics.

The peak current values at different scan rates were used to derive the D_{Zn} according to Randles-Sevcik equation16:

$$i_P = (2.69 \times 105)n^{3/2}AD_{Zn}^{1/2}C_{Zn}Liv^{1/2} \quad (4)$$

where iP is the peak current, n is the charge-transfer number, A is the geometric area of the active electrode, D_{Zn} is the Zn_{2+} ion diffusion coefficient, C_{Zn} is the concentration of zinc ions in the electrode, and v is the scan rate.

Diffusion coefficient D-value testing was conducted using the formula:

$$D = \frac{R^2T^2}{2S^2n^4F^4C^4\,\sigma^2} \quad (5)$$

where R represents the gas constant (R = 8.314 $J \cdot mol^{-1} \cdot K^{-1}$), F denotes Faraday's constant (96485.33 $C \cdot mol^{-1}$), S signifies the contact area between positive and negative electrodes (S = 1.13·cm^2), n represents the number of electron transfers, C stands for electrolyte concentration, and σ represents the slope obtained from conductivity curves Z' and w as shown in equation below, where Z' represents resistance and ω represents angular frequency(ω=2πf):

$$Z' = Rs + Rct + \sigma\omega^{-1/2} \quad (6)$$

3.3 Simulation details

The active sites of the APIPP for energy storage were determined through theoretical calculations (DFT), which were conducted using Gaussian software.[3] All of the molecular configurations were optimized at B3LYP level of theory with 6-311d(g) basis set, and the Gibbs free energy was calculated at M062X level of theory with /def2TZVP basis set with a solvation model (SMD) in water solution[4, 5]. All the calculated results of the molecular electrostatic potential (MESP) were carried out by Multiwfn 3.3.9 programs and the visualizations were performed by Visual Molecule Dynamics (VMD) software.[6]

4. Details of costing

The cycling stability of the APIPP electrode material deserves attention, given its potential as a commercially viable solution for large-scale energy storage in battery compositions. Based on the conducted tests, it can be inferred that the energy density of the APIPP electrode material at a current density of 5 A is 71.62 $Wh \cdot kg^{-1}$, indicating that storing 1 kWh of electricity would require approximately 13.96 Kg of active material. Extrapolating from twenty thousand cycles, the estimated cost of APIPP amounts is 0.0087~0.0090 dollars per circle. The specific calculation process is as follows:

At a current density of 5 $A \cdot g^{-1}$, the energy density is 71.62. To prepare 1 kilowatt-hour (1 kWh), 13.96 kilog of APIPP (Molar Volume: 520.26) are required, with a synthesis yield of 65%. The synthesis of 41.27 mol of the product requires a 1:1.2 ratio of PD and DAP, comprising 41.27 mol of PD (DAP1 + protocatechualdehyde 1.25) and DAP 49.54. Ultimately, 51.59 mol of protocatechualdehyde (7125 g) and 90.794 mol of DAP are necessary. The synthesis of DAP requires oPD as a raw material, with a yield of 39.85%. A total of 455.66 mol of DAP, equivalent to 49274.93 g, need to be synthesized. The synthesis process involves oxidation catalysis by ferric chloride

hexahydrate, with a consumption of 0.574 g. For the synthesis of oPD, 50 milliliters of 0.08M ferric chloride hexahydrate (4E-3 mol, 1.0812 g) is needed, totaling 26057 * 1.0812 = 92813 g. The cost of oPD (31.11 $), 3,4-dihydroxybenzaldehyde (95376 $), and ferric chloride hexahydrate (38.98 $) totals 165.78 yuan for the synthesis of APIPP. Considering a 5% to 10% increase in cost due to losses of other liquids, calculated over 20,000 cycles, the cost per cycle ranges from 0.0087 to 0.0090 USD.

5. Experimental data

Table S1 Comparison of the functional group utilization efficiency of APIPP electrode with other active materials in AZIBs.

Organic cathode material	Functional group utilization efficiency	Remarks Content	references
This work	93%	Imidazole, free amino and hydroxyl groups	
TQD	75.19%	Having free hydroxyl groups (-OH)	7
TAHQ	44.80%		8
TPHAPT	68.36%		9
PTONQ	62.08%		10
PTO-4NH2Ph	83.61%		11
HATTA	72.45%	Nanoparticle size	12
C8Q	46.35%		13
PM12	30.98%		14
PT12	46.41%		14
NT12	56.01%		14
PMTP@CNT-40	74.02%	The CNT was added	15
rPOP	37.64%		16
PQN14	52.63%		17
NI-DAQ	60.73%		18
DAP	85.92%	free amino groups	19
2D-PT-COF	52.66%		20
2D-NT-COF	86.44%		20
TAHNTN	51.61%		21

Selected as a benchmark for comparison are various organic compounds that have been utilized as positive electrode materials in recent years. The objective is to evaluate the efficiency of functional group utilization in these materials. It has been noted that compounds exhibiting remarkably high rates of functional group utilization are those that incorporate single-walled carbon nanotubes and oxidized/reduced graphene, as well as those composed of molecular particles at a very small scale. It is noteworthy that materials with functional groups such as amino and imidazole exhibit a high utilization rate of these functional groups. In comparison to these materials, the specially designed APIPP stands out for its exceptional utilization rate of active

functional groups at the submicron level, leveraging the inherent properties of its functional groups.

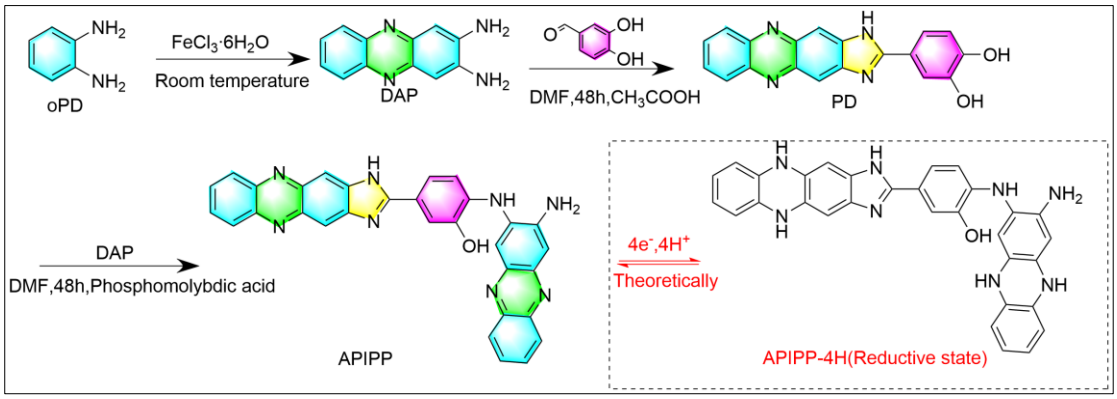

Scheme S1. The synthesis route of APIPP and corresponding redox process.

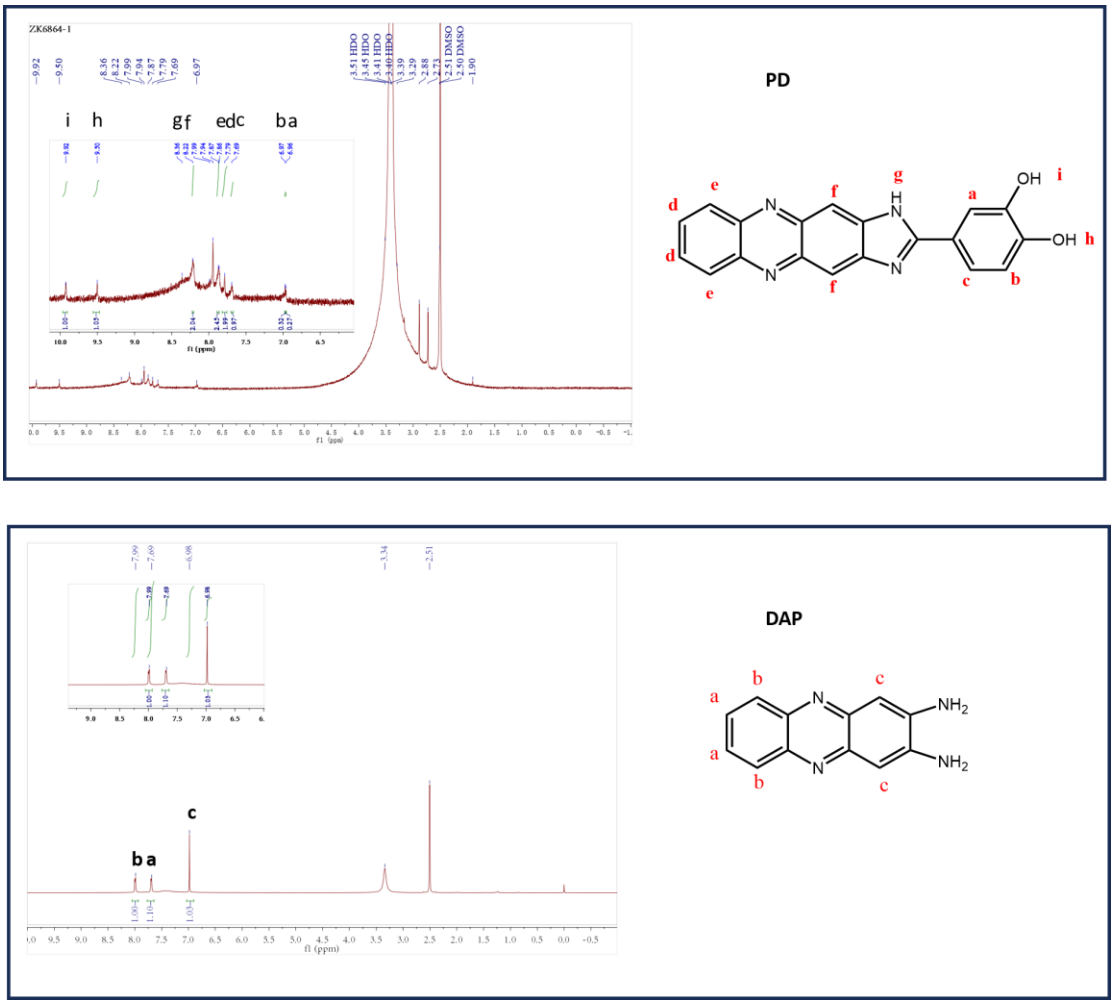

Figure S1. The ^{1}H NMR of PD and DAP.

The NMR hydrogen spectrum test graph of the intermediate PD was processed using MestReNova, and the NMR results are as follows PD. ^{1}H NMR (600 MHz, DMSO-d_6) δ 9.92

(s, 1H), 9.50 (s, 1H), 8.36 (s, 1H), 8.22 (s, 2H), 7.89 – 7.86 (m, 2H), 7.79 (s, 2H), 7.69 (s, 1H) , 6.97 (s, 1H), , 6.96 (s, 1H). Indicating the successful preparation of PD

the NMR results are as follows DAP. ^{1}H NMR (600 MHz, DMSO-d6) δ 7.99 (s, 1H), 7.69 (s, 1H), 6.98 (s, 1H).

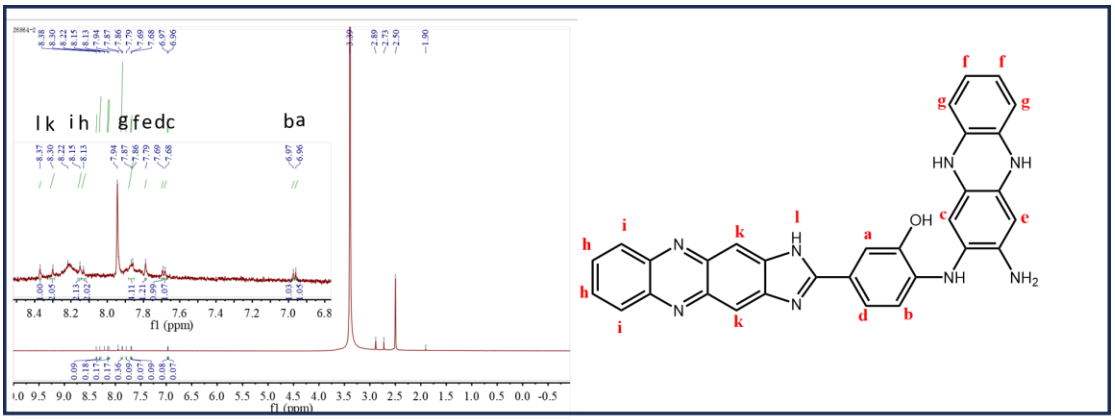

Figure S 2 The ^{1}H NMR of APIPP.

The NMR hydrogen spectrum test graph of the intermediate APIPP was processed using MestReNova, and the NMR results are as follows APIPP. (1H NMR (600 MHz, DMSO-d6) δ 8.37 (s, 1H), 8.30 (s, 2H), 8.15 (s, 2H), 8.13 (s, 2H), 7.86 (d, J = 5.0 Hz, 4H), 7.79 (s, 1H), 7.69 (s, 1H), 7.68 (s, 1H), 6.97 (s, 1H), 6.96 (s, 1H).)

In the aforementioned NMR hydrogen spectrum, apart from the peaks of deuterated DMSO and the material, there are still some impurity peaks. Specifically, peaks at 2.73, 2.89, and 7.94 in both PD and APIPP are due to the solvent DMF used in the synthesis process, while the peak at 3.4 is attributed to methanol used during the washing process. In APIPP, the broad peak at 8.21 is due to a small amount of intermediate PD residue, which has a higher solubility than APIPP, thus appearing as a broad peak in the NMR. It is worth mentioning that the theoretical specific capacity of PD is only 163 mAh g^{-1}, which does not elevate the specific capacity of APIPP material.

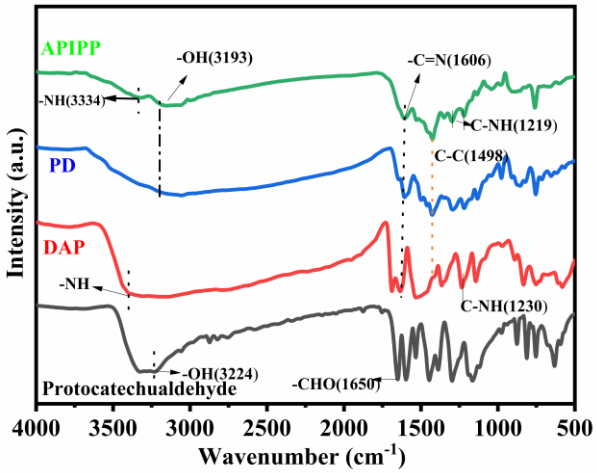

Figure S3. The FT-IR of APIPP, PD, DAP and Protocatechualdehyde.

For DAP, a characteristic peak corresponding to the -NH_2 group is observed at

approximately 3390 cm^{-1}, along with another peak around 1230 cm^{-1} representing the C-NH_2 group. The stretching vibrations of the pyrazine ring skeleton are evident at positions 1689 and 1645, respectively. while a distinctive peak at 1606 cm^{-1} signifies the pyrazine ring skeleton group. The key indicator of successful synthesis of PD compared to DAP is the disappearance of the -NH_2 vibration peak, and the appearance of the -OH vibration peak at 3193 cm^{-1}.[1, 2]

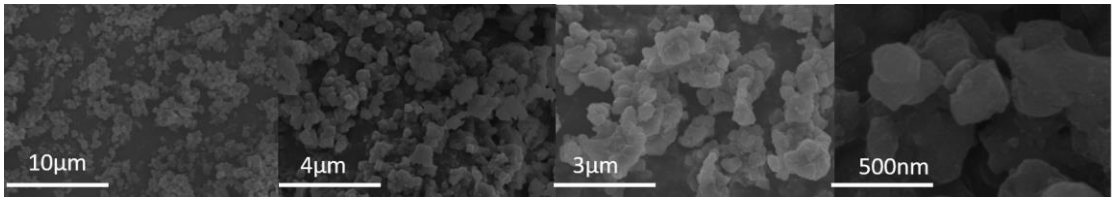

Figure S4. The spatial configuration of APIPP molecules under the scanning electron microscope.

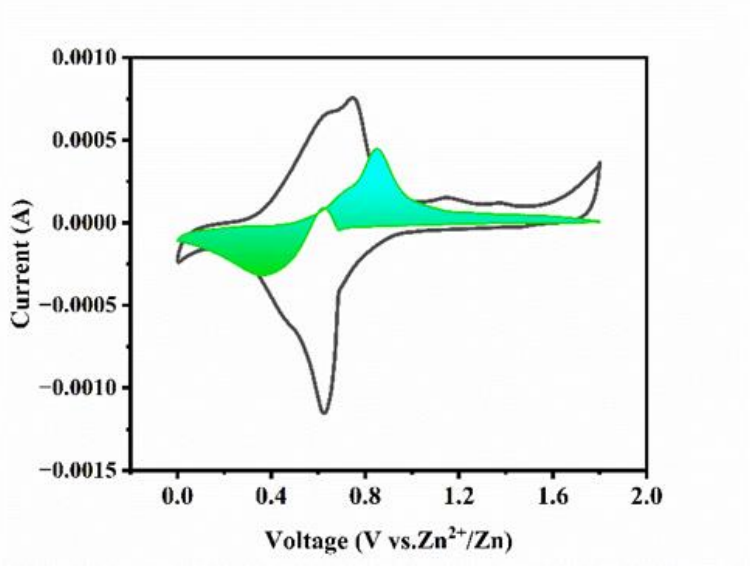

Figure S5. Pseudo-capacitance fitting plot at a scan rate of 0.2 mV·s^{-1}.

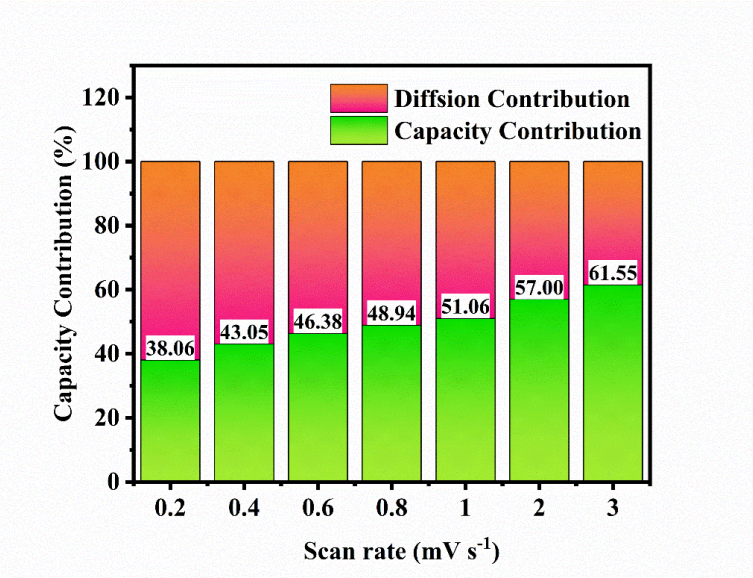

Figure S6. The plot between log(current(mA)) and log (Scan rate (mV s^{-1}), and the calculation of b values.

The graph illustrates the area of pseudo-capacitive and actual capacity contributions. It can be observed that at low scanning speeds, the pseudo-capacitive contribution is minimal, predominantly controlled by diffusion. This provides evidence for the diffusion control of APIPP molecules in aqueous zinc ion batteries.

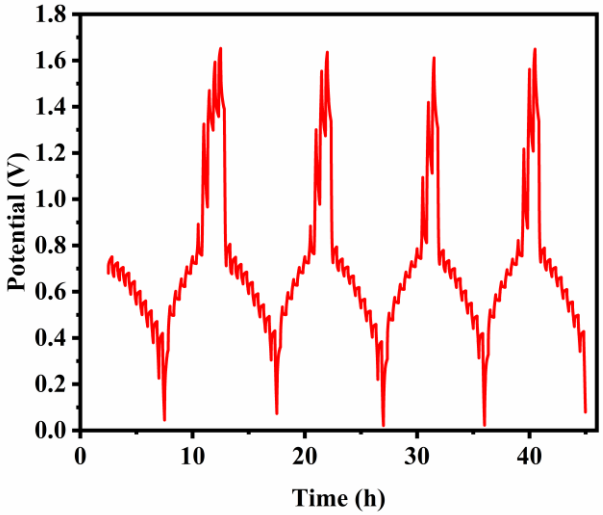

Figure S7. Fitting lines of Z' and ω-1/2 correspond to the Nyquist plots at a) origin b)100 cycle numbers of the TPHATP electrode.

The ion diffusion coefficient (D) is calculated by galvanostatic intermittent titration technique (GITT) measurement according to the following equation:

$$D = \frac{4L^2}{\pi\tau}\left(\frac{\triangle E_s}{\triangle E_t}\right)^2 \quad (7)$$

Where τ is the relaxation time. ΔEs is the steady-state voltage change after the current pulse. ΔEt is the voltage change during the relaxation process. L is the ion diffusion length (cm), approximately equal to the thickness of active material (54 μm). by employing peak current values at various scan rates and deriving D_{Zn} using the Randles-Sevcik equation, we found that the diffusion coefficients measured by the Galvanostatic Intermittent Titration Technique (GITT) lie within the 10^{-7} and 10^{-8} range. Compared to reported cathode materials, this demonstrates a superior performance, highlighting the material's significant advantages in ion diffusion kinetics.

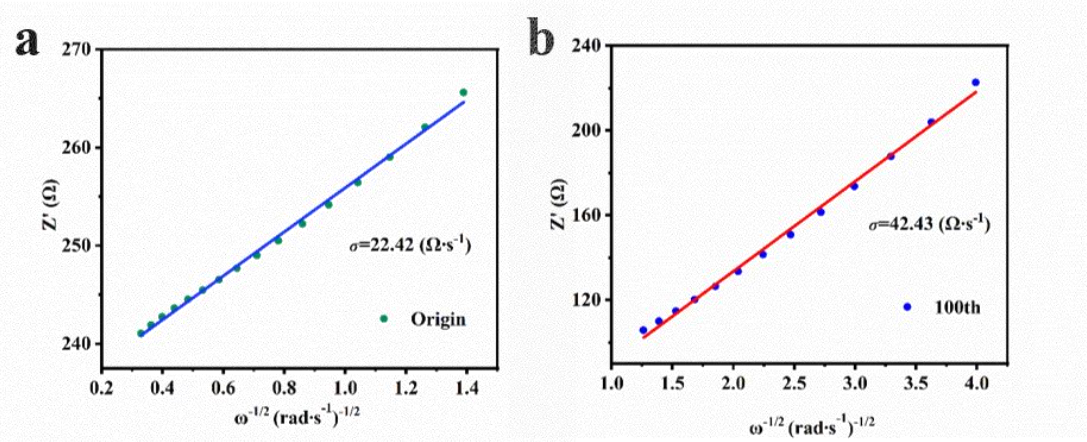

Figure S8. Fitting lines of Z' and $\omega^{-1/2}$ correspond to the Nyquist plots at **a)** origin **b)**100 cycle numbers of the TPHATP electrode.

The slope σ was determined by fitting the equation (5), starting with an initial value of 22.42 and reaching a value of 42.43 after the 100 th iteration (Figure S9), which can be attributed to the dominant diffusion-controlled chemical kinetics behavior.

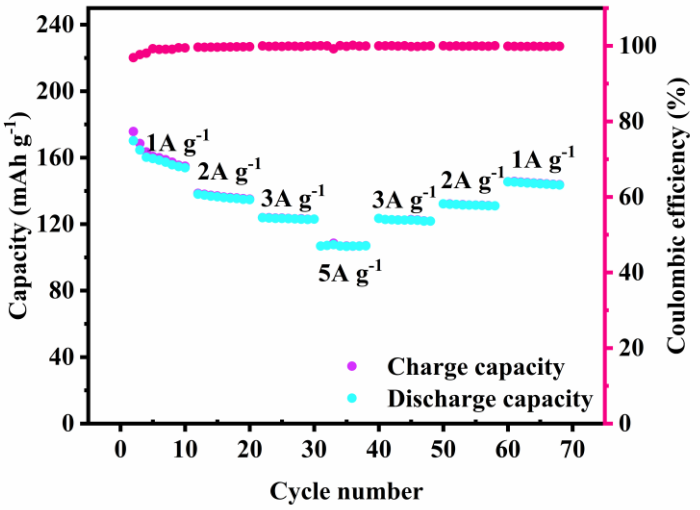

Figure S9. Rate performance at different current density.

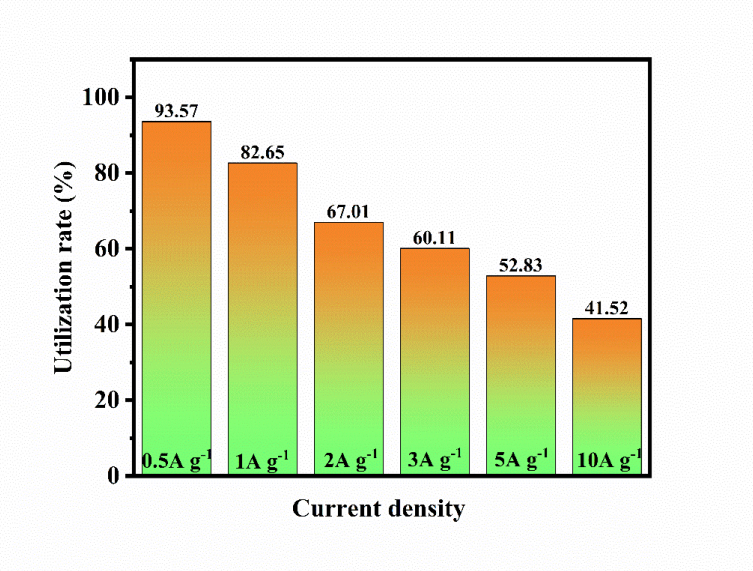

Figure S10. Specific capacity utilization at different current densities.

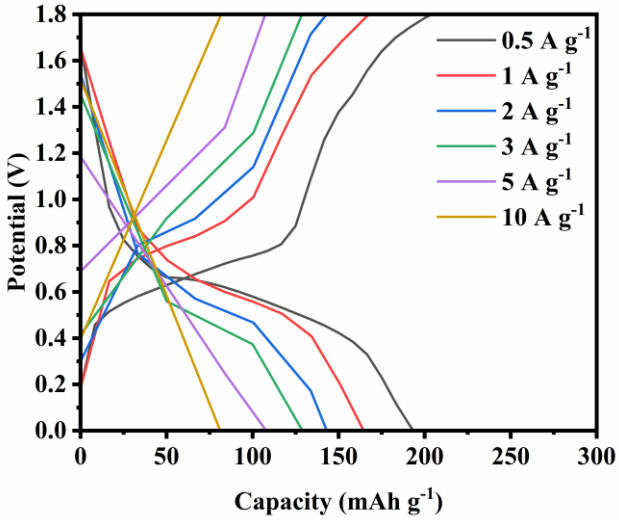

Figure S11. Rate performance at different current density.

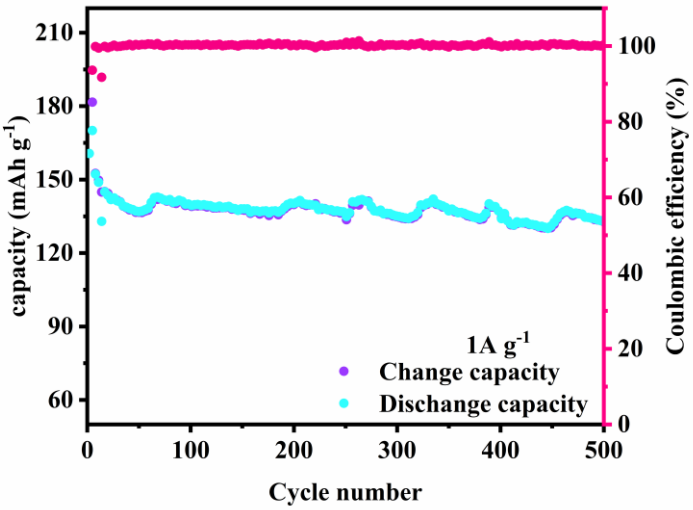

Figure S12. Cycling stability and coulombic efficiency of APIPP at 1 A·g^{-1}.

The cycle stability of the APIPP cathode material was evaluated through long-term cycling tests at 1 A·g^{-1}. **Figure S12** illustrates the results of the long-term cycling test conducted at a current density of, with an initial specific capacity of 160.6 mAh·g^{-1}. After the first 20 cycles, there was a rapid decrease in capacity which stabilized at 143.6 mAh·g^{-1}, remaining constant even after 500 cycles, resulting in a capacity retention rate of 93.0% compared to the 20 th cycle.

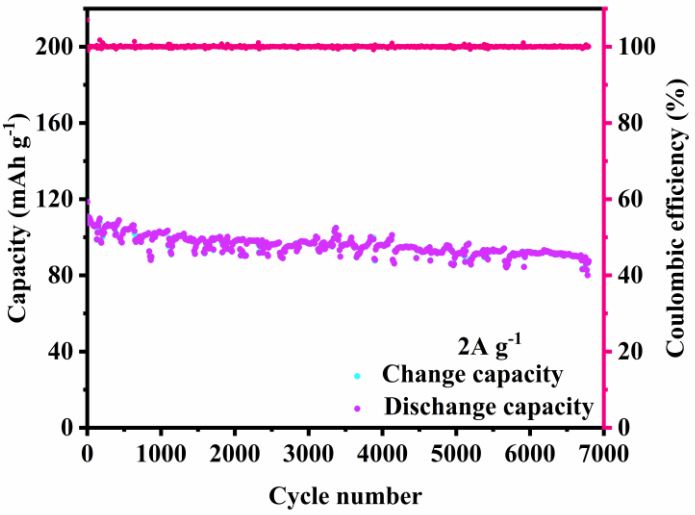

Figure S13. Cycling stability and coulombic efficiency of APIPP at 2 A·g^{-1}.

The cycle stability of the APIPP cathode material was evaluated through long-term cycling tests at 2 A·g^{-1}. **Figure S13**illustrates the results of the long-term cycling test conducted at a current density of, with an initial specific capacity of 110.7 mAh·g^{-1}. remaining constant even after 7000 cycles, resulting in a capacity retention rate of 79.0%.

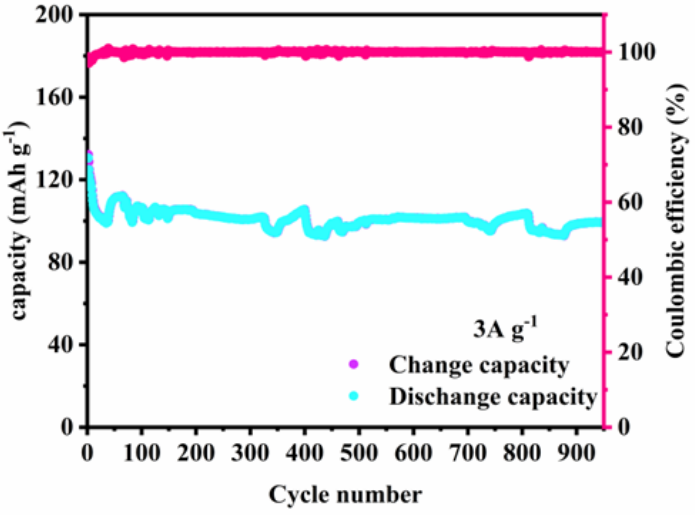

Figure S14. Cycling stability and coulombic efficiency of APIPP at 3 A·g^{-1}.

The cycle stability of the APIPP cathode material was evaluated through long-term cycling tests at 3 A·g^{-1}. **Figure S14** illustrates the results of the long-term cycling test conducted at a current density of, with an initial specific capacity of 132.1 mAh·g^{-1}. After the first 20 cycles, there was a rapid decrease in capacity which stabilized at 103.1

mAh·g^{-1}, remaining constant even after 7000 cycles, resulting in a capacity retention rate of 96.9%.

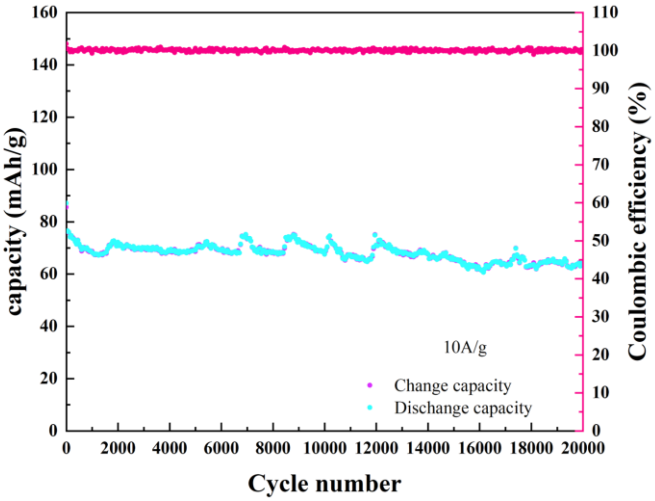

Figure S15. Cycling stability and coulombic efficiency of APIPP at 10 A·g^{-1}.

The cycle stability of the APIPP cathode material was evaluated through long-term cycling tests at 10 A·g^{-1}. **Figure S15** illustrates the results of the long-term cycling test conducted at a current density of, with an initial specific capacity of 85.5 mAh·g^{-1}. remaining constant even after 20000 cycles, resulting in a capacity retention rate of 74.38%.

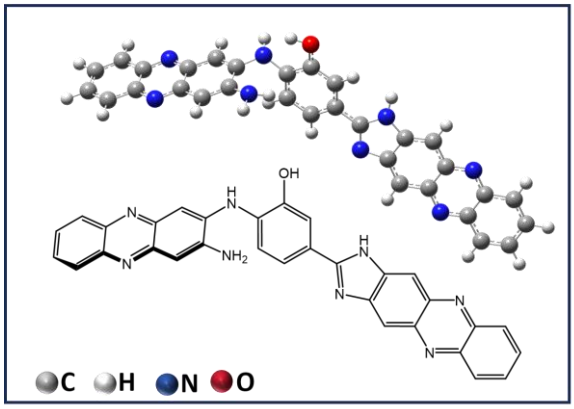

Figure S16. Optimized molecular structure model and corresponding molecular structural formula in theoretical simulation calculations.

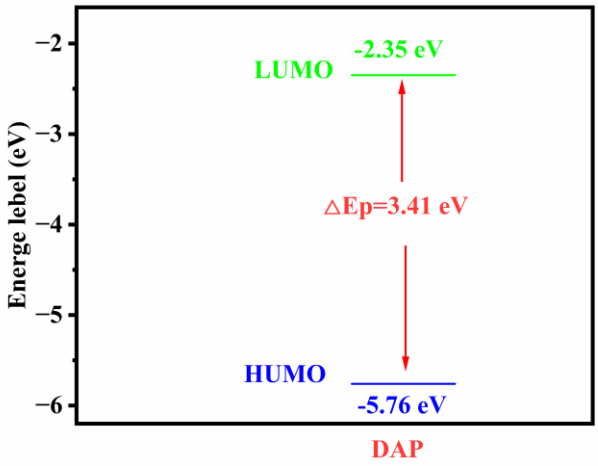

Figure S17. The LUMO and HOMO calculation graphs of DAP molecules were obtained through DFT.

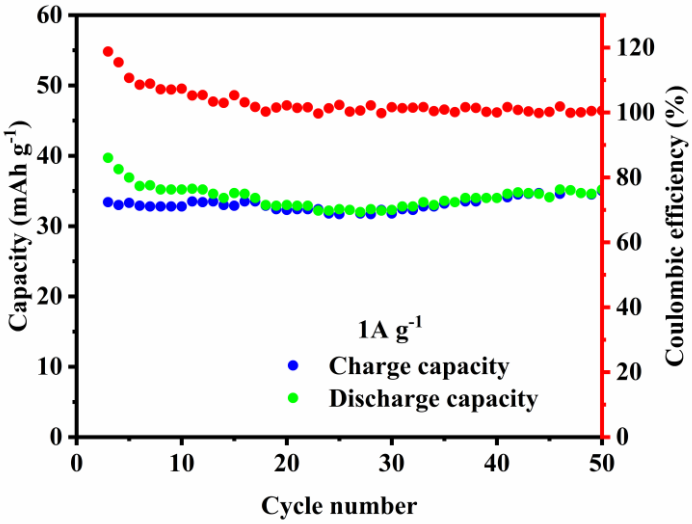

Figure S18. The APIPP electrode material underwent extensive cycling tests in a 1 M $Zn(OTF)_2$ in acetonitrile electrolyte at a current density of 1 $A \cdot g^{-1}$.

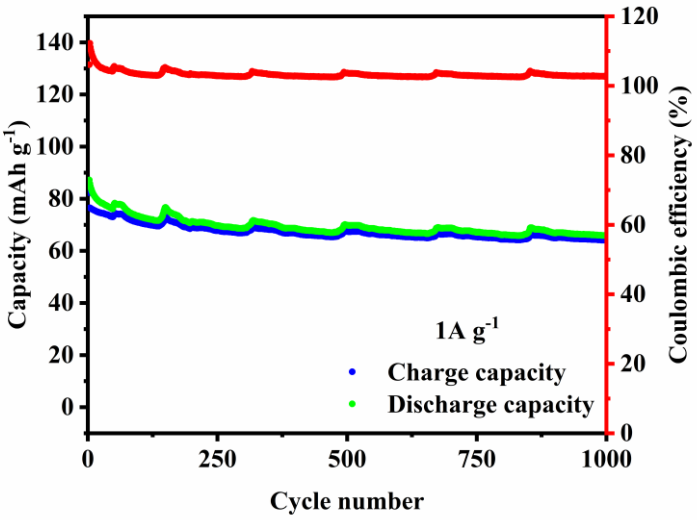

Figure S19. The APIPP electrode material underwent extensive cycling tests in a 2 M H_2SO at a current density of 1 $A \cdot g^{-1}$.

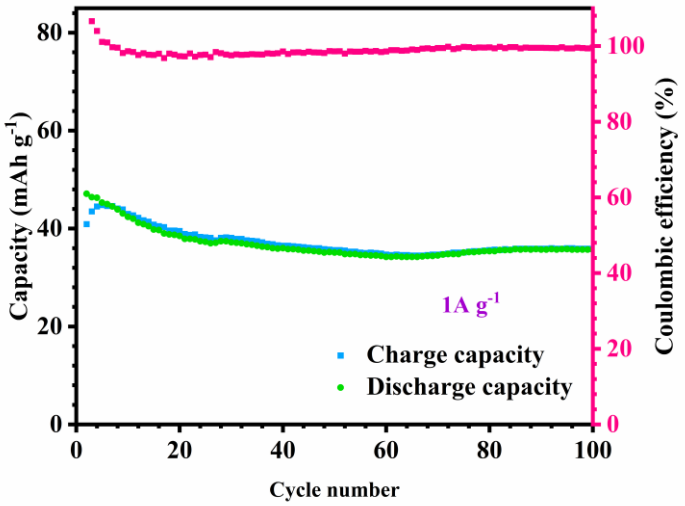

Figure S20. The APIPP electrode material underwent extensive cycling tests in a 1 M Na_2SO_4 at a current density of 1 $A \cdot g^{-1}$.

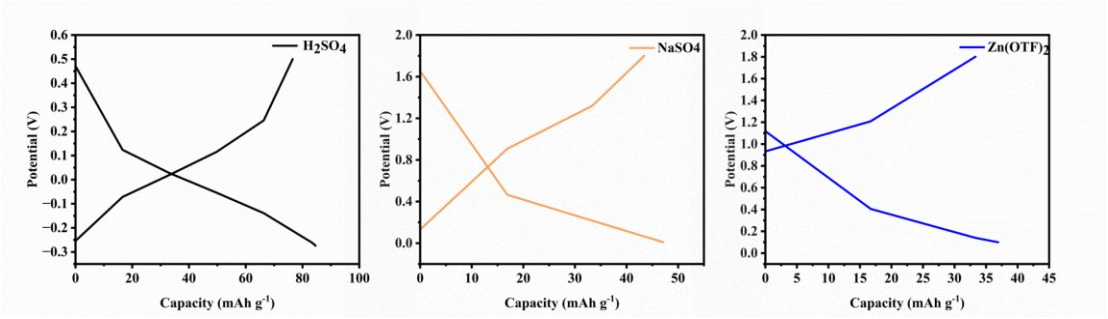

Figure S21. Charge and discharge curves of APIPP in three different electrolytes

We constructed a three-electrode system utilizing APIPP to perform charge-discharge

tests in a 2 M sulfuric acid solution (**Figure S18**). The capacity contribution at a current density of 1 $A \cdot g^{-1}$ was determined to be 87.15 $mAh \cdot g^{-1}$, which was almost half of the battery employing $ZnSO_4$ solution as the electrolyte that exhibited a capacity of 158.06 $mAh \cdot g^{-1}$ under the same current density. This indicates again the same ion shuttle mechanism between the two systems but the different capacity contribution. It can be speculated that the protonation of pyrazine or 2H-pyrazine may have suppressed the contribution of the second pair of active groups. Moreover, when conducting coin battery tests using a 1 M $Zn(OTF)_2$ in acetonitrile (**Figure S19**), only a capacity contribution of 32 $mAh \cdot g^{-1}$ was observed, consistent with cyclic voltammetry results and suggesting only the surface functionalities work. This substantiates the involvement of H^+ ions as energy storage ions during charge-discharge processes. Additionally, tests with 1M $NaSO_4$ resulted in a capacity of only 43 $mAh \cdot g^{-1}$(**Figure S20**), likely due to the low concentration of H^+. These results demonstrate that without the H^+ generated from the hydrolysis of hydrated zinc ions, the battery cannot achieve practical specific capacity, thereby validating the role of Zn^{2+} in the proton storage process of the material.

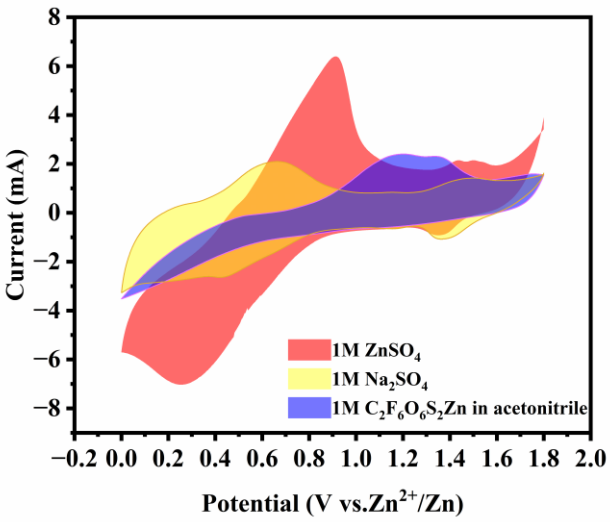

Figure S22. CV curves under different electrolyte conditions.

The ion storage mechanism of the APIPP electrode material was further investigated through experimental analysis (**Figure S22**). CV tests were conducted on the APIPP electrode under various electrolyte conditions. To eliminate interference from H^+ in aqueous solutions, 1 M zinc trifluoromethanesulfonate0 ($Zn(OTF)_2$) in acetonitrile was used for controlling test, and the absence of distinct reductive peak indicates that Zn^{2+} may not play a role in energy storage. When tested with 1 M Na_2SO_4 electrolyte, clear redox peaks emerged but much lower than using $ZnSO_4$ aqueous solution as an electrolyte, suggesting that H^+ produced by hydrolysis of zinc sulfate is indeed involved in energy storage during charge-discharge process.

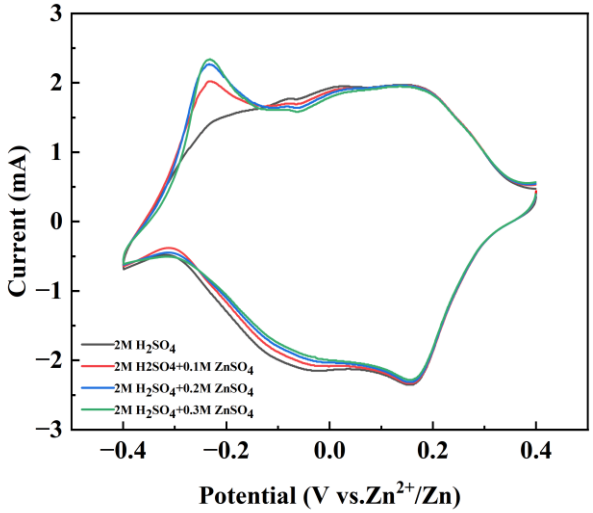

Figure S23. CV curves of different concentrations of Zn^{2+} and 2 M H_2SO_4 as electrolyte.

To gain a comprehensive understanding of the role played by Zn^{2+}, we conducted an experiment involving gradual addition of $ZnSO_4$ into a 2 M H_2SO_4 electrolyte (**Figure S23**) to observe the variation of cyclic voltammetry (CV). It is evident that only a discernible reduction peak was observed with solely H_2SO_4, however, with the introduction of $ZnSO_4$, a distinct oxidation peak appeared at -0.25 V (V vs Ag/AgCl), but there was no significant change in the overall CV area, indicating that Zn^{2+} is not an active ion for energy storage. This finding aligns with the reported energy storage mechanism involving pyrazine rings in aqueous zinc ion batteries[9]

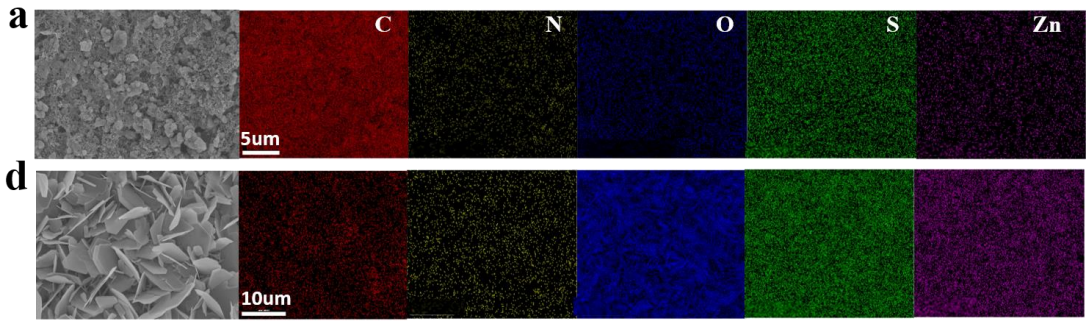

Figure S24 a) Scanning electron microscope (SEM) images and mapping of the APIPP cathode in a fully charged state. **b)** Scanning electron microscope (SEM) images and mapping of the APIPP cathode in a fully discharged state.

In **Figure S24**b, under full discharge state, the SEM and mapping images show the formation of numerous lamellar zinc sulfate hydroxide on the surface of the positive electrode, accompanied by a significant presence of elements such as S, O, Zn. Conversely, in **Figure S24**a, under full charge state, the lamellar zinc sulfate hydroxide disappears and the elemental signals weaken.

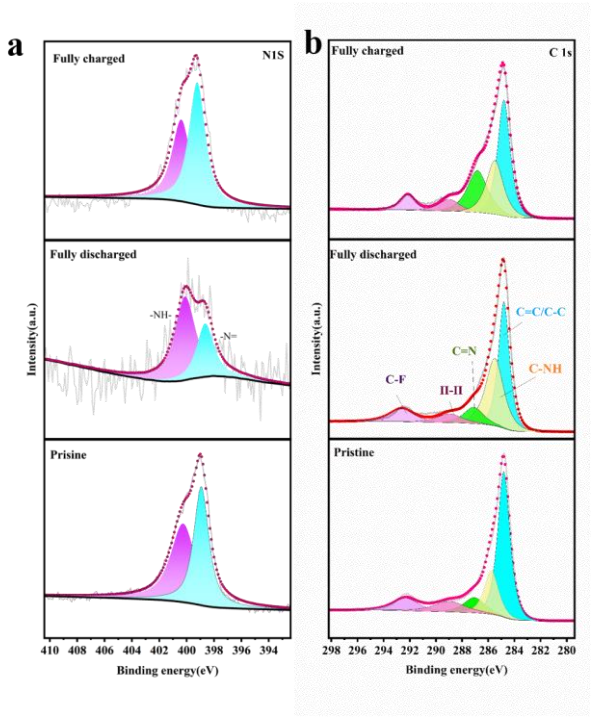

Figure S25 a) N 1s XPS of APIPP electrode at different charge–discharge states and b) C 1s XPS spectra of APIPP electrode at pristine, fully discharged and fully charged processing.

The C 1s spectrum exhibits multiple peaks, including the C=C/C-C of aromatic ring at 284.80 eV, the -C-NH- group of dihydro-pyrazine at 285.43 eV,[22] the -C=N- bond of pyrazine at 287. 11eV,[23] the π-π stacking interaction with APIPP molecule at 289 eV,[24] and the C-F bond originating from adhesive (PTFE) at 292.59 eV.

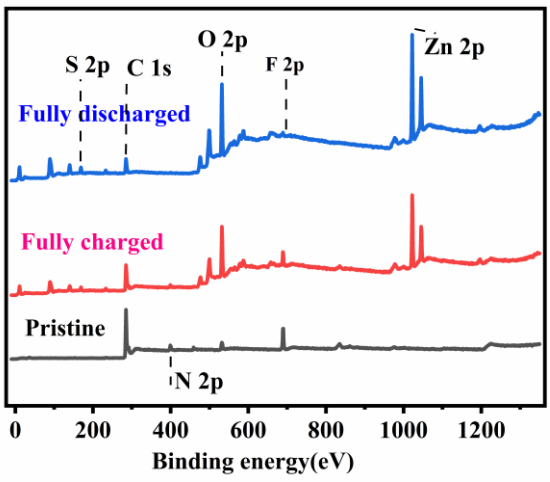

Figure S26. XPS full spectrum analysis of APIPP electrode films in different states.

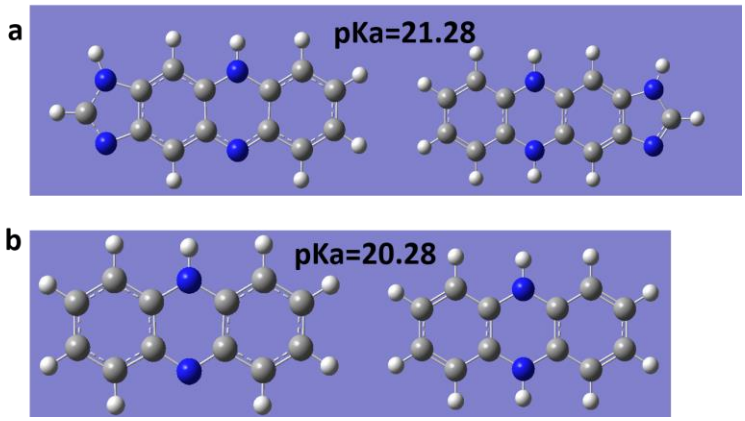

Figure S27. Theoretical simulation of phenazine-like molecules

To further investigate the existence of Zn-APIPP adducts during discharge, we performed additional DFT. breaking down APIPP into phenazine-imidazole and phenazine structural units, and calculated the pKa of their reduced states. During discharge, the pyrazine portion of both units loses aromaticity to become dihydropyrazine. The removal/absorption of H^+ or Zn^{2+} during energy storage can be determined by the pKa of H^+ in anti-aromatic dihydropyrazine groups. If H^+ participate, the discharge product is in NH form; if Zn^{2+} participate, the product is N-Zn, forming a nitride with Zn^{2+} and N^-. Generally, nitrides are too basic to exist stably in aqueous solutions and should rapidly hydrolyze to form NH, indicating H^+ storage in redox reactions.Thus, we calculated the pKa values of fully reduced dihydropyrazine units, with results showing values of 21.28 and 20.28 for the two structural units, both much higher than water's pKa（15.75）. This indicates that H2O is more acidic than APIPP, meaning these N- cannot exist in aqueous solutions. This calculation is independent.

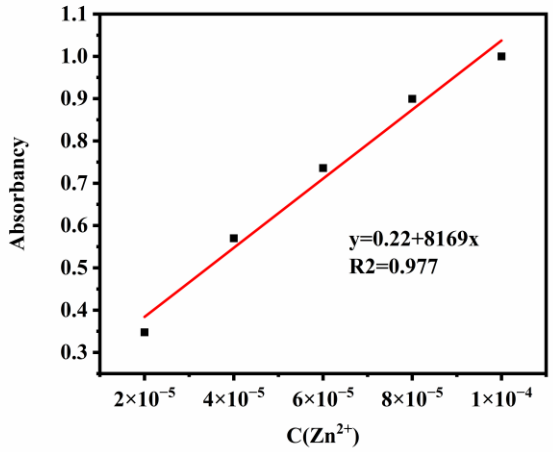

Figure S28. $ZnSO_4$ atomic absorption standard curve

We applied APIPP to a film, weighing 5.16 mg of active material, and paired it with a zinc electrode in an excess 2M zinc sulfate electrolyte. After 10 charge-discharge cycles, the APIPP electrode was discharged to 0.01V, then soaked in 50 mL of 2M H_2SO_4 solution for 20 minutes to remove surface basic zinc sulfate. The electrolyte was then

replaced with 30 mL of 1M sodium sulfate solution, and the electrode was charged to 1.8V to investigate if zinc ions entered the material during energy storage. Atomic absorption spectroscopy showed an absorbance of 2.5 for the sodium sulfate electrolyte after charging, corresponding to a concentration of approximately 0.0002791 mol L^{-1} in 30 mL, which is on the same order of magnitude as the concentration of 0.00066 mol L^{-1} if all zinc from the 5.16 mg APIPP material was embedded in the $NaSO_4$ solution. This confirms that zinc ions did enter the material and participate in the energy storage process. XPS analysis, showing no N-Zn bond, along with the lower specific capacity in zinc triflate electrolyte, indicates that zinc ions coordinate with the material rather than being embedded for energy storage.

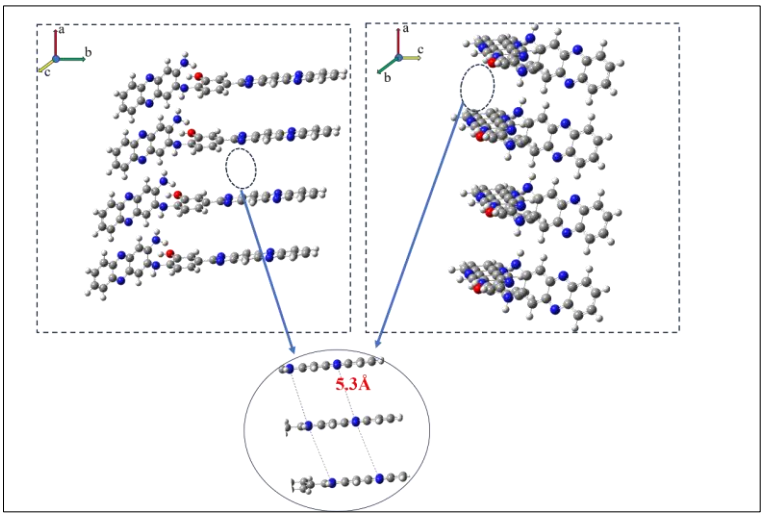

Figure S29. the interlayer spacing of molecular stacking as calculated through DFT. The calculations indicate that $Zn(H_20)_6^{2+}$ cannot directly shuttle between the materials and must desolvate before entering. Combined with the atomic absorption spectroscopy results, a small amount of Zn^{2+} (0.074nm)can shuttle within the material for non-energy storage coordination.

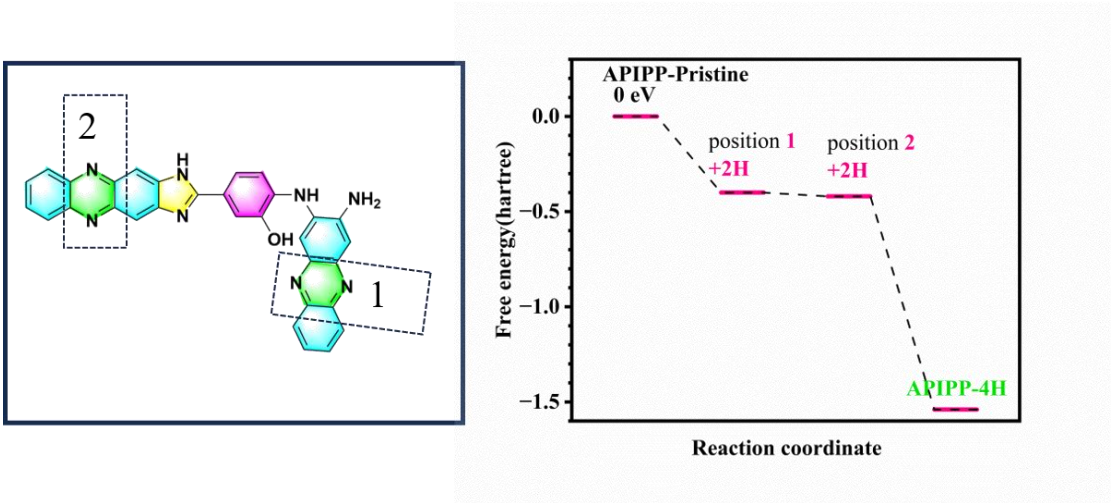

Figure S30. Determining the Gibbs free energy associated with proton insertion into various pyrazine rings of the APIPP electrode material through Density Functional

Theory (DFT) calculations.

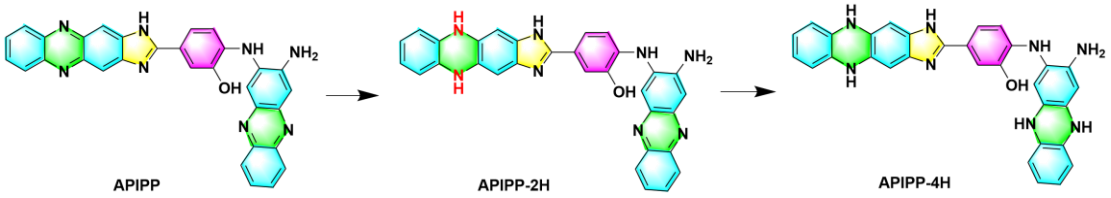

Figure S31. Schematic of the H+ reaction steps in APIPP electrode material.

References

1. S. R. Pour, A. Abdolmaleki and M. Dinari, *J. Mater. Sci.*, 2019, **54**, 2885-2896.
2. X.-N. Qi, H.-Q. Dong, H.-L. Yang, W.-J. Qu, Y.-M. Zhang, H. Yao, Q. Lin and T.-B. Wei, *Photochem. Photobiol. Sci.*, 2020, **19**, 1373-1381.
3. M. J. Frisch, G. Trucks, H. B. Schlegel, G. E. Scuseria, Robb, J. R. Cheeseman, G. Scalmani, V. Barone, B. Mennucci and G. A. Petersson, 2009.
4. S. Hu, T. Li, M. Huang, J. Huang, W. Li, L. Wang, Z. Chen, Z. Fu, X. Li and Z. Liang, *Adv. Mater.*, 2021, **33**, 2005839.
5. A. V. Marenich, C. J. Cramer and D. G. Truhlar, *J. Phys. Chem. B*, 2009, **113**, 6378-6396.
6. T. Lu and F. Chen, *J. Comput. Chem.*, 2012, **33**, 580-592.
7. S. Menart, K. Pirnat, D. Pahovnik and R. Dominko, J. Mater. Chem. A, 2023, **11**, 10874-10882.
8. Y. Wang, S. Niu, S. Gong, N. Ju, T. Jiang, Y. Wang, X. Zhang, Q. Sun and H.-b. Sun, *Small Methods*, 2024, 2301301.
9. S. Niu, Y. Wang, J. Zhang, Y. Wang, Y. Tian, N. Ju, H. Wang, S. Zhao, X. Zhang, W. Zhang, C. Li and H.-b. Sun, *Small*, 2023, 2309022.
10. T. Sun, Z. Yi, W. Zhang, Q. Nian, H. J. Fan and Z. Tao, *Adv. Funct. Mater.*, 2023, **33**, 2306675.
11. T. Sun, W. Zhang, Q. Nian and Z. Tao, *Chem. Eng. J.*, 2023, **452**, 139324.
12. J. Li, L. Huang, H. Lv, J. Wang, G. Wang, L. Chen, Y. Liu, W. Guo, F. Yu and T. Gu, *ACS Appl. Mater. Interfaces*, 2022, **14**, 38844-38853.
13. C. Ding, Y. Wang, C. Li, J. Wang, Q. Zhang and W. Huang, *Chem. Sci.*, 2024, **15**, 4952-4959.
14. J. Wang, H. Lv, L. Huang, J. Li, H. Xie, G. Wang and T. Gu, *ACS Appl. Mater. Interfaces*, 2023, **15**, 49447-49457.
15. Y. Liu, Z. Li, C. Li, Y. Wei, S. Yan, Z. Ji, S. Zou, H. Li, Y. Liu, C. Chen, X. He and M. Wu, *Chem. Eng. J.*, 2024, **488**, 150778.
16. O. Buyukcakir, R. Yuksel, F. Begar, M. Erdogmus, M. Arsakay, S. H. Lee, S. O. Kim and R. S. Ruoff, *ACS Appl. Energy Mater.*, 2023, **6**, 7672-7680.
17. C. Guo, Y. Liu, J. Zhang, W. Zhao, K. Wang, M. Su, Y. Hu and L. Wang, *Ionics*, 2023, **29**, 2319-2328.
18. Q. Feng, Y. Cao, C. Guo, L. Chen, W. Sun and Y. Wang, *ACS Appl. Energy Mater.*, 2023, **6**, 7899-7907.
19. J. Liang, M. Tang, L. Cheng, Q. Zhu, R. Ji, X. Liu, Q. Zhang, H. Wang and Z. Liu, *J. Colloid Interface Sci.*, 2022, **607**, 1262-1268.
20. Y. Liu, Y. Lu, A. Hossain Khan, G. Wang, Y. Wang, A. Morag, Z. Wang, G. Chen, S. Huang, N. Chandrasekhar, D. Sabaghi, D. Li, P. Zhang, D. Ma, E. Brunner, M. Yu and X. Feng, *Angew. Chem., Int. Ed.*, 2023, **62**, e202306091.
21. X. Chen, H. Su, B. Yang, X. Liu, X. Song, L. Su, G. Yin and Q. Liu, *Chin. Chem. Lett.*, 2024, **35**, 108487.
22. R. Gao, Q. Zhang, H. Wang, F. Wang, J. Ren, X. Wang, X. Ma and R. Wang, *J. Energy Chem.*, 2023, **79**, 1-11.
23. H.-K. Lee, J. Park, I. Kim, H.-D. Kim, B.-G. Park, H.-J. Shin, I.-J. Lee, A. P. Singh, A. Thakur and J. Y. Kim, *J. Phys. Chem. C*, 2012, **116**, 722-725.
24. A. Cano, J. Rodríguez-Hernández, A. Shchukarev and E. Reguera, *J. Solid State Chem.*, 2019, **273**, 1-10.